Stabilisation of aragonite: the role of Mg^{2+} and other impurity ions

Matthew Boon[1], William D.A. Rickard[2], Andrew L. Rohl[3], and Franca Jones[1]*

Affiliation:
[1] *Curtin Institute for Functional Molecules and Interfaces, School of Molecular and Life Sciences, Curtin University.*
[2]*John de Laeter Centre, Curtin University.*
[3] *Curtin Institute for Computation, Curtin University.*

*Mail: Curtin University, GPO Box U1987, Perth, Australia 6845.

Email: F.Jones@curtin.edu.au Phone: 618 9266 7677

KEYWORDS: aragonite, stability, impurities, magnesium.

ABSTRACT: Aragonite formation and stabilisation in seawater is still an area of active investigation since the thermodynamically stable product at room temperature is calcite. In this manuscript, purely inorganic systems that were found to stabilise aragonite were analysed by various techniques. Dynamic Light Scattering was used to characterise the nucleation behaviour of the system and it was found that the presence of magnesium ions during crystal formation inhibits nucleation overall, not just calcite nucleation. In addition, it was found that sulfate is not necessary to stabilise aragonite. Microanalysis by energy dispersive X-ray spectroscopy (EDS) and electron backscatter diffraction (EBSD) revealed that the aragonite that was formed had a disordered core with, sodium, magnesium and sulfate ions incorporated into the structure. To the best of the authors' knowledge this is the first time an ACC core in aragonite has been visualised in a completely abiotic, synthetic system (in the absence of organic molecules). Inclusion of these impurities into the structure may explain the stability of aragonite in natural seawaters.

Calcium carbonate is known to have several different forms. Monohydrocalcite ($CaCO_3.H_2O$) and ikaite ($CaCO_3.6H_2O$) are hydrated crystalline structures that tend to be formed at low temperatures,[1–4] while the other hydrated form is amorphous (amorphous calcium carbonate, ACC) and can contain varying amounts of water.[5] ACC is thought to be an important precursor to the formation of calcite,[6,7] through a non-classical crystallisation pathway and the presence of Mg ions has been found to stabilize ACC.[8] Calcite, aragonite and vaterite are all anhydrous crystalline calcium carbonate structures. Calcite is trigonal (a = 4.9896 Å, c = 17.061 Å),[9] aragonite is orthorhombic (a = 4.9611 Å, b = 7.9672 Å, c = 5.7407 Å)[10] and vaterite is hexagonal (a = 4.13 Å, c = 8.49 Å)[11] (see Figure 1). The thermodynamic stability of these anhydrous forms follows the order calcite>aragonite>vaterite[12] at room temperature and pressure.

Calcium carbonate is an important biomineral, with many marine organisms utilising calcium carbonate minerals for skeletal or protective features.[13–15] Not surprisingly, therefore, it is of interest to materials scientists who wish to understand how to create and control material properties for technological applications. In addition, calcium carbonate is gaining interest from a CO_2 sequestering perspective.[16–18] If carbon dioxide can be converted to carbonate and reacted with calcium, CO_2 can be effectively sequestered as mineral deposits, potentially helping to mitigate global warming.[19,20] Examples of this strategy can be found in the literature.[21,22]

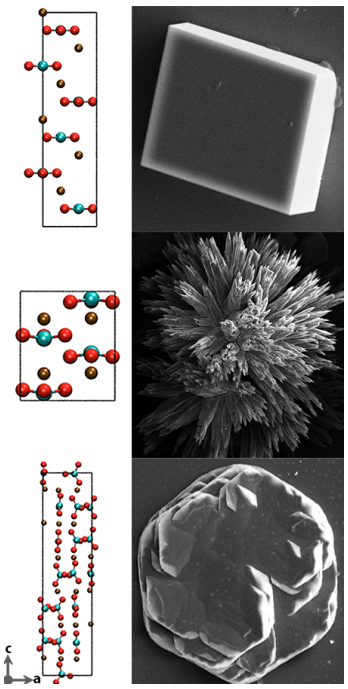

Figure 1. Crystal structure and electron microscopy images showing the typical morphology of (top) calcite, (middle) aragonite and (bottom) vaterite (one possible structure).[11]

While the thermodynamically stable form of calcium carbonate at room temperature and pressure is calcite, in seawater aragonite is often observed.[23,24] Originally, the existence of aragonite was thought to be due to stabilisation and involvement of biologically derived organic material[25,26] as much of the literature on nacre can attest. However, there is evidence to show that aragonite can be stabilised in the absence of organics ([27] and this work). This raises the question as to why this occurs. One hypothesis is based on the surface free energy. The relationship between nucleation rate and surface free energy (see Eqn 1), assuming that supersaturation is constant, is that the lower the surface free energy the higher the nucleation rate.

$$J = A \exp[(-B\gamma^3/\sigma^2)] \qquad \text{–(Eqn 1)}$$

Where J is the nucleation rate, A is the pre-exponential factor, B is a constant that incorporates various other constants such as temperature, Boltzman's constant etc., γ is the surface free energy and σ the supersaturation.[28]

In seawater, the presence of Mg^{2+} can increase the surface free energy of one or both forms and thereby lower the nucleation of this/these solids.[29] The hypothesis proposed is that Mg^{2+} ions adsorb and cause the surface free energy of calcite to increase[30] while it is assumed that Mg^{2+} ions do not change the surface free energy of aragonite. Consequently, aragonite would nucleate first and the increased surface free energy of the Mg-calcite limits the subsequent formation of calcite.[30] This literature[31] also proposes that the presence of magnesium ions increases the solubility of Mg-calcite. However, Mg containing calcite has been found to have a solubility curve that decreases initially with Mg content before increasing (Figure 2 from [32]). Now, not only must surface free energy be considered but also an increase in supersaturation.

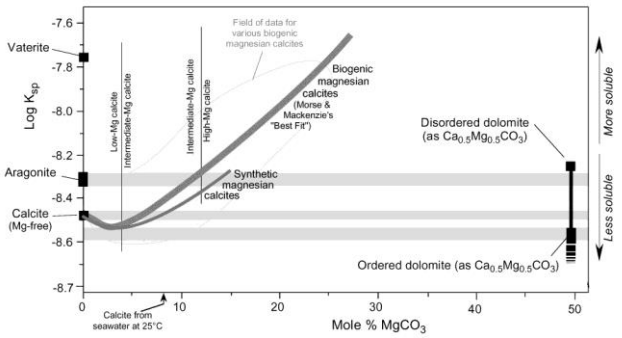

Figure 2. Solubility of calcite versus Mg content.[32]

Kawano et al.[33] assumed a surface free energy for calcite of 120 mJ/m^2 [34] while aragonite was assumed to have a surface free energy of 150 mJ/m^2 [35]. However, even if we take the average surface energy for calcite with Mg^{2+} incorporation as 500 mJ/m^2 this does not explain the lack of calcite formation. Heterogeneous nucleation can require much less of a driving force than homogenous nucleation thus, calcite should form on appropriate surfaces.[36] In essence, an increase in surface free energy while possibly causing a slower transformation to calcite does not adequately explain the stabilisation of aragonite in seawater. In other words, it does not explain why the aragonite does not dissolve and form calcite over a long time period.

Another hypothesis is that the presence of sulfate is also required. Sulfate has been thought to inhibit calcite formation more than aragonite formation and therefore aragonite is observed in seawater. More recently, it is thought sulfate ions have a synergistic effect with Mg^{2+} ions.[37] Others[30,38,39] suggest that Mg^{2+} ions alone can stabilise aragonite formation (and this work).

Generally, all previous hypotheses have focused on surface adsorption mechanisms with the consensus being that as aragonite is the denser structure it does not incorporate Mg^{2+} ions or sulfate ions to any extent. However, recent literature has shown that Mg^{2+} ions can incorporate into aragonite[40,41] although these manuscripts did not link this incorporation to the increased stability of the aragonite in seawater. In addition, previously thought spectator ions such as sodium are slowly being shown to be critical components to various biominerals.[40]

This work investigated two aspects of aragonite formation. The first was to examine the aragonite formed from a complex mixture that mimics many of the seawater components and physically characterise the solids formed. The second aim was to use computational information in an effort to better understand incorporation processes that may occur. In addition, an investigation into what factors are critical for aragonite stabilisation was undertaken. Note that in this study, calcium carbonate was formed under homogenous nucleation conditions and different mechanisms may apply for heterogeneous nucleation. The $Ca:CO_3$ ratio was held constant at 1:1 and the solids were then characterised using several methods including infrared, Raman, microscopy and diffraction techniques.

Materials and Methods

All materials used were of analytical grade and used as received. Ultrapure water (resistivity > 18 MΩ cm at 22 ^{0}C) was used in preparation of all solutions.

Synthetic Seawater (SSW) solution: The SSW solution ion concentrations were modeled after Berges[42] . The stock and final solution concentrations are shown in Table 1 and further experimental details can be found in the supplementary information (Section 1).

Table 1: Synthetic seawater (SSW) salt solutions (without Mg ions present)

Species	Stock Concentration (mM)	Final Concentration (mM)
NaCl	3,630	363.0
Na_2SO_4	250	25.00
KCl	80	8.04
KBr	7.25	0.725
H_3BO_3	3.72	0.372
NaF	0.657	0.0657
$SrCl_2$	0.82	0.082

To know which phases are going to crystallise out from solution, the program pHREEQC[43] was used to calculate the saturation index (SI). The SI is calculated using equation 2, where a_i, $a_j \ldots a_n$ refer to the activity of species i, j,...n, and the K_{sp} is the solubility product of the solid species.

$$SI = \log\left[\frac{(a_i \times a_j \times \ldots a_n)}{K_{sp}}\right] \quad \text{–(Eqn 2)}$$

All experiments were prepared to achieve an SI for calcite of 2.0. A list of all the final concentrations for each of the experiments discussed in this manuscript can be found in the supplementary information (Section 1). The solid phases with an SI value greater than 0 can be found in Table 2. Phases with a value less than 0 are not expected to crystallise as they are understaturated. Clearly, calcite is expected to form, as is aragonite, while dolomite is not (despite the high SI) due to the lack of this mineral forming at ambient temperatures.[44] Strontianite may form but the low supersaturation means that, if it is observed, it is most likely due to heterogeneous nucleation.

Table 2. Solid phases with SI greater than zero

	SI	log K_{sp}^{pHREEQC}
Aragonite	1.86	-8.336
Calcite	2.00	-8.480
Dolomite	4.39	-17.09
Strontianite	0.29	-9.271

Crystallisation Morphology: Determination of the calcium carbonate morphology was achieved *via* static batch crystallisation experiments in triplicates. Concentrations of $CaCl_2$ and $NaHCO_3$ needed to achieve a calcite saturation of 2.00 were determined using PHREEQC[45] for each of the solution compositions (supplementary information, Section 1). A fresh bicarbonate stock solution was prepared and all salt solutions were adjusted to pH 8 using NaOH (0.1 and 1 M) and HCl (0.1 and 1 M) before the commencement of the batch crystallisation experiments. In the control batch experiment, the required concentration of $CaCl_2$ to achieve the desired final concentration was added to a clean glass vial followed by the addition of water and a glass cover slide. The solution was left at room temperature for ½ hr before the addition of $NaHCO_3$ solution to achieve the desired final concentration. The vial was then capped and left at room temperature for 3 days. After 3 days (or the desired time) the glass cover slide was removed from the solution and rinsed using a small amount of water to wash away residual salt. The cover slide was then prepared for imaging.

For batch experiments involving the addition of ions ($MgCl_2$, SSW), these were added after the $CaCl_2$ and water, and left to equilibrate for ½ hr before the addition of the $NaHCO_3$ solution. While the initial pH was adjusted to be 8 for all experiments the pH after ≥ 3 days was found to be 7.6 ± 0.1 (measured by a calibrated Orion pH meter).

The polymorph of individual particles was confirmed, if necessary, by obtaining a Raman spectrum using a Witech Confocal Raman instrument (50x objective, 10 accumulations, 50 msec collection per accumulation and 4cm^{-1} resolution).

Powder X-ray Diffraction (XRD): The method used above in the 20 mL vial batch experiments was scaled to a volume of 4 L to obtain sufficient solids for analysis. The solutions were stirred for 3 hours before being left at room temperature (22 ^{0}C) for 7 days without stirring. While the initial pH is 8 after this time period the pH was found to be 7.6. After the 7 days, the solids were filtered through a 0.45 µm membrane and washed multiple times with water before being dried in a desiccator. An internal standard of fluorite (~10 wt.% mass) was mixed into the sample and homogenized to achieve a uniform particle size distribution. XRD patterns were obtained on a Bruker D8 Advance instrument using Cu K_α radiation. The samples were rotated at 30 rpm, with a working 2θ range of 15 – 120 degrees at a step size of 0.001^0 and a divergence slit of 0.3^0. The patterns were then fitted using Topas software to get the quantitative phase content and the lattice parameters. All fitted data is shown in the supplementary information (Section 4).

Mounting of sample in resin and milling: Solids obtained from the 4 L crystallisation experiment was placed in a mould with Epofix epoxy resin poured over the sample while under vacuum to ensure the sample was impregnated with the resin. The sample was then mechanically polished using a Stuers Tegramin-30 and a range of cloth grains for various amounts of time. Once mechanically polished the sample was then exposed to ion beam milling to achieve a fine polish.

Scanning Electron Microscopy (SEM): Images were captured using a Zeiss EVO SEM with an attached energy dispersive x-ray spectrometer (EDS) to enable elemental analysis of the samples. Samples for imaging were prepared by placing the glass cover slides from the batch crystallisation experiments onto SEM stubs using carbon tape. Liquid graphite was applied to the edges of the glass cover slide, and a platinum coating (~ 5 nm) was sputtered onto the samples to reduce charging effects.

Electron backscatter diffraction (EBSD): Microstructural analysis by EBSD mapping was conducted on the resin mounted sample using a Tescan MIRA3 FESEM operated at an accelerating voltage of 20 kV, 70˚ sample tilt, a working distance of 20 mm and a beam current of 5 nA. EBSD patterns were collected with a Nordlys Nano high-resolution detector. The EBSD data were acquired with the Oxford Instruments AZtec version 2.3 software. The whole-grain map was collected with a 200 nm step size, while the high-resolution map had a 50 nm step size. The EBSD data was processed with the Oxford Channel5 software. Further information can be found in the supplementary information (Section 2).

Fourier transform infrared (FTIR): A Nicolet iS50 FT-IR fitted with an attenuated total reflection (ATR) single bounce diamond crystal was used. The diamond crystal was cleaned with ethanol and a background was captured before each run. Spectra were collected between 4000–700 cm^{-1} with a resolution of 4 cm^{-1} and 64 scans were captured for each spectrum, lasting ~1 minute by adding a small amount of solid onto the ATR crystal and then using the in-built attachment to make sure the solids made contact with the ATR crystal. FTIR spectra were collected at least twice on each sample.

Dynamic Light Scattering (DLS): DLS was used to investigate the nucleation behaviour of different calcium carbonate systems, using a Malvern NanoZS instrument. The instrument calculates the derived counts of the system under investigation, quoted in kilocounts per second (kcps), and is related to the number of particles scattering light in the incident volume. Particle counts below 100 kcps corresponded to the solution only. A rapid rise in counts represents a nucleation event occurring. Higher counts correspond to greater numbers of nuclei.

Identical solutions to the batch morphology experiments were prepared, however, the final volume was 50 mL. For example, for the control sample the calcium chloride stock solution was added to water (to achieve the desired final concentration) before the bicarbonate stock solution was added to commence crystallization. The solution was continuously stirred at 250 rpm with an aliquot taken every 3 minutes for the duration of the 30 minute experiment. Each DLS experiment was repeated three times and the average counts determined.

Transmission Electron Microscopy (TEM): Samples for TEM analysis were extracted from specific sites from the polished sample in resin using a focused ion beam (FIB)-SEM. A Tescan Lyra3 FIB-SEM with a Ga^+ ion source was operated at 30 kV for the lift out and mounting of the lamellas onto Cu TEM grids. The lamellas were then thinned to 100 nm with the final thinning step performed with low voltage to reduce beam damage. The TEM analysis was carried out on a FEI Talos F200X field emission gun (FEG) transmission electron microscope (TEM). Analyses were performed using bright field imaging in TEM, selected area electron diffraction and scanning TEM, which included EDS.

Molecular modeling

The molecular modeling of Mg and/or sulfate incorporation into the structures of calcite and aragonite was implemented using the same principles as a previous publications[46]. The potentials for the ions were taken from previous literature[47,48]. In short, a crystal simulation cell of the appropriate solid was created in GDIS[49] and the size was chosen such that it was close to cubic in the three lattice directions by multiplying the lattice parameters appropriately. Mg^{2+} and SO_4^{2-} were then substituted for a Ca^{2+} and/or CO_3^{2-} ion respectively. The potentials and their values for Mg^{2+} and SO_4^{2-} are given in the supplementary information (Section 3) and are used without modification from [48]. GULP[50] was then used to minimise the total energy. Several configurations were trialled to try to determine the global minima. The replacement energy was then calculated for each crystal structure according to the chemical reaction that applied:

For Mg substitution:

$$CaCO_{3(s)} + nMg^{2+}_{(aq)} \rightarrow Mg_nCa_{1-n}CO_{3(s)} + nCa^{2+}_{(aq)} \quad \text{–(Eqn 3)}$$

$$E_{repl} = (E_{final} + nE_{hyd\,Ca} + nE_{Ca}) - (E_{init} + nE_{hyd\,Mg} + nE_{Mg}) \quad \text{–(Eqn 4)}$$

For $MgSO_4$ substitution the sulfate was purposely put in the vicinity of the magnesium ion (to replicate the notion that the two were incorporating simultaneously) and so not all possible sulfate locations were simulated. However, the replacement energy was similarly calculated to Mg substitution:

$$CaCO_{3(s)} + nMg_{(aq)} + nSO_4^{2-}{}_{(aq)} \rightarrow Mg_nCa_{1-n}(SO_4)_n(CO_3)_{1-n(s)} + nCa^{2+}{}_{(aq)} + nCO_3^{2-}{}_{(aq)} \quad \text{–(Eqn 5)}$$

$$E_{repl} = (E_{final} + nE_{hyd\,Ca} + nE_{hyd\,carb} + nE_{Car\,\&\,Ca}) - (E_{init} + nE_{hyd\,Mg} + nE_{hyd\,Sulf} + nE_{Sulf} + nE_{sulf\,\&\,Mg}) \quad \text{–(Eqn 6)}$$

Where E_{repl} is the replacement energy, E_{final}, E_{init} is the final and initial energy respectively, E_{Ca} etc. is for the isolated ion in the gas phase and E_{hyd} is the hydration energy for the ions. There is also a term for sulfate due to its non-point-like structure (-20 eV per sulfate). The more negative the replacement energy the more thermodynamically favourable is the replacement.

RESULTS

Morphology

The results of crystallisation experiments in the presence of Mg^{2+} and common seawater ions is consistent with previously reported literature.[51,52] A mixture of calcite and aragonite is formed when high Mg^{2+} ion concentrations are present (see results of XRD, FTIR, Table 3 and Figure 3). The addition of Mg^{2+} increases the amount of aragonite formed ~24% when in pure water. The calcite morphology is significantly altered from that expected in pure water while that of aragonite is not (compare Figure 3a to Figure 3b[23] and Figure 1 for the aragonite morphology). EDX spectral analysis of these results suggested that the aragonite appeared to have Mg associated with it (Figure 3). This result, however, could be due to the analysis zone (spot size) of the EDX. Thus, further investigation was necessary.

Table 3. Solids determined by Rietveld % by mass (see supplementary Section 4)

	Calcite	Aragonite	Amorphous
Control	90.83	Not found	9.17
Control+ Mg	53.50	24.02	22.48
SSW	78.08	0.82	21.10
SSW + Mg	23.42	56.90	19.68

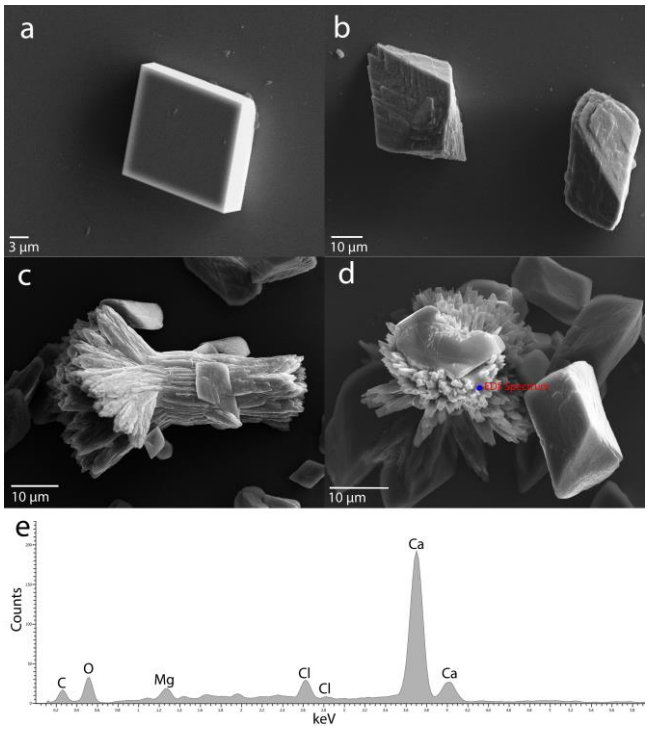

Figure 3. (a) SEM image of calcium carbonate formed in pure water, (b) SEM image of calcite particles formed in the presence of SSW + Mg^{2+} (c) SEM image of aragonite particle formed in the presence of SSW + Mg^{2+} (d) SEM image of particles showing where the EDX spectrum in (e) was taken.

Characterisation of the solids formed in the presence of Mg^{2+} Infrared

The infrared spectra for particles formed in the presence of SSW solutions show that aragonite only forms and persists when Mg^{2+} ions are present (Figure 4, aragonite diagnostic peak is a doublet at 700 and 713 cm^{-1}).

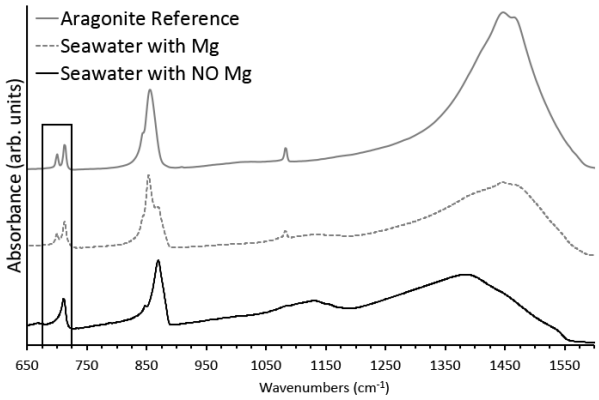

Figure 4. FTIR spectra of solids formed in SSW with and without magnesium ions (mole fraction of Mg^{2+} present in solution is 0.612)

In pure water it was found that vaterite (diagnostic peak 740 cm^{-1}, Figure 5) was stabilised at high sulfate concentrations (>20mM) but as the amount of Mg^{2+} concentration was increased more and more aragonite appeared with vaterite disappearing and calcite also substantially reducing (observed through reduction of the 870 cm^{-1} peak, Figure 5). Of interest is a noticeable sulfate band (broad peak at 1000-1200 cm^{-1}, Figure 4 & 5) suggesting significant incorporation of sulfate into one or more of the calcium carbonate polymorphs. The peak at ~1080cm^{-1} is not diagnostic as it is found in many carbonates. Vaterite kinetic stabilisation due to sulfate has been previously observed and so this data supports those findings[53].

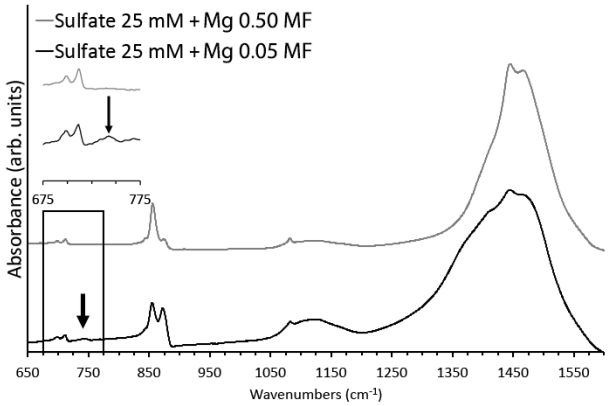

Figure 5. FTIR spectra of solids obtained in the presence of magnesium ions (at different molar fraction, MF) when 25 mM sulfate is also present. Arrow shows presence of vaterite peak.

Nucleation

While light scattering by particles is a convolution of both particle size and number, particle counts as determined by light scattering techniques can be used to give an indication of nucleation rates provided significant aggregation is avoided. Simply put, since a homogenous solution is present before crystallisation occurs a low count is expected prior to nucleation and then a high particle count is expected post nucleation (particularly if a single nucleation event is assumed to occur).

As can be seen in Figure 6, the presence of Mg^{2+} ions in pH 8 water (with NaCl) appears to lead to lower particle numbers suggesting a decrease in the nucleation rate. This is expected from previous literature that suggests the presence of Mg^{2+}ions inhibits calcite nucleation.[37,38,54] However, if aragonite nucleation is not impacted by the presence of Mg^{2+} ions then there should still be a nucleation event for the aragonite particles. Thus, the observed behaviour does not appear to be based on aragonite nucleating at the expense of calcite but is indicative of an overall inhibition of nucleation.

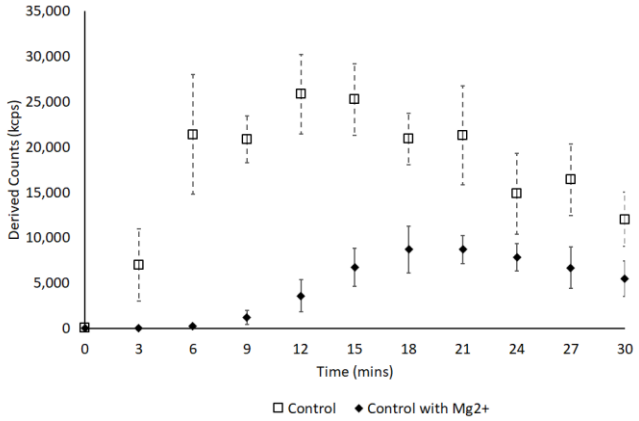

Figure 6. Derived counts versus time for calcium carbonate produced in water+NaCl (control) and water+NaCl+Mg ions (control + Mg). Vertical lines represent variation from average calculated

In SSW (without magnesium ions present), the nucleation rate is almost half that observed in the 'control' despite the same SI (see Figure 7). This is due to ions such as strontium – known to inhibit calcium carbonate formation.[55] There is a delay in nucleation when magnesium ions are present, similar to that in Figure 6.

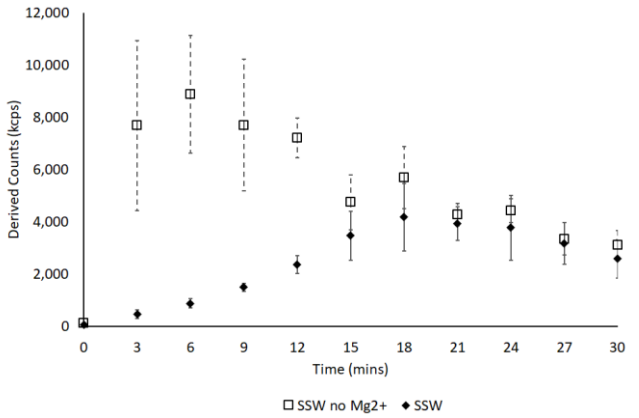

Figure 7. Derived counts versus time for calcium carbonate produced in SSW with and without Mg^{2+} ions. Vertical lines represent variation from average calculated

In the absence of Mg^{2+} ions nucleation is essentially over after 3 min. When Mg^{2+} ions are present there does not appear to be a single nucleation event but rather nucleation occurs over a prolonged time-period (~15 minutes). This occurs both in the presence and absence of the other impurity ions. This *may* indicate 'nucleation' *via* a transitory phase such as ACC since Mg^{2+} ions are known to stabilise ACC.[8] This amorphous solid *may* lead to the situation where as crystalline particles are formed and released into solution an increasing particle count results.

Phase Analysis

XRD revealed that the solids formed in pH 7.6-8 water after 7 days are calcite (Figure 8). Using Rietveld refinement the only crystalline phases found were fluorite (internal standard) and calcite, which accounted for >90 wt.% thus there was <10wt.% amorphous content (Supplementary information, Section 4). The addition of Mg^{2+} ions into this system resulted in a higher amorphous content as well as the formation of aragonite (Table 3.). The 'control' samples contain no sulfate, thus the stabilisation of aragonite is *not* dependent on any synergistic effect of sulfate with magnesium. Comparison of the 'SSW + Mg^{2+}' with the 'control + Mg^{2+}' suggests that the presence of sulfate (and/or other) ions increases the amount of aragonite formed. The amorphous content is similar in % terms to the case where magnesium ions only are present. Unfortunately, XRD cannot give much information on disordered phases, therefore, the microstructure of the 'SSW + Mg^{2+}'solids was further investigated *via* other methods.

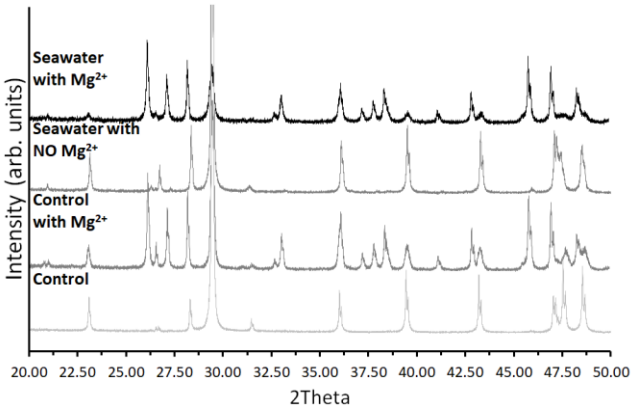

Figure 8. XRD patterns of solids formed for control conditions, control conditions with Mg^{2+} ions, SSW and in SSW with Mg^{2+} ions (the mole fraction of Mg2+ ions when present was 0.612)

Microstructure of precipitated particles

Microstructural analysis by EBSD revealed that calcite grains decorate the exterior of the aragonite particles (Figure 9). This suggests that calcite is formed after the aragonite (due to dissolution/re-crystallisation processes) as would be expected by Ostwald's rule of stages.[28] Interestingly the core of the aragonite particle had poor EBSD pattern band contrast and a low rate of indexation by the software. In EBSD analysis this indicates poorly crystalline or amorphous material. The presence of a poorly ordered/amorphous core has been previously observed, for example, aragonite particles in both coral[56,57] and mollusc shells[58–60] show disordered core regions. It is thought to arise from the aggregation of ACC followed by the crystallization of ACC to aragonite by a solid-state transition. To the best of the author's knowledge, however, this is the first time an ACC core has been observed in a completely abiotic, synthetic system devoid of organic solvents.

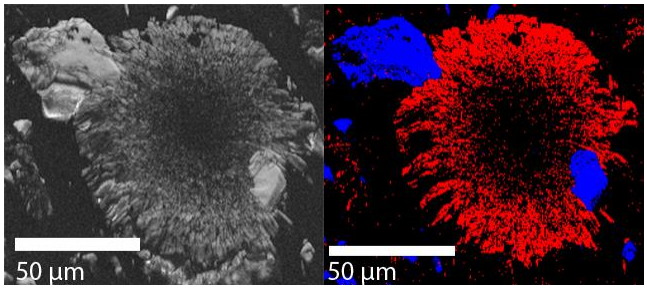

Figure 9. (left) SEM Backscatter image and (right) overlaid phases detected from EBSD analysis for solids formed in SSW+Mg^{2+}.

The chemical composition of the particles using EDS was mapped simultaneously during EBSD analysis (Figure 10). Ca and O were present in all particles (Supplementary information, Section 2, Sup-Fig 1) confirming it to be calcium carbonate. Unusually, Na and S are observed in both aragonite and calcite particles and, although present at low levels, Mg is above background levels in aragonite despite previous assumptions.[61] The high levels of Mg and S in the calcite particles do support a synergistic incorporation of these ions as suggested by Nielsen et al.[37] The presence of Na in both calcite and aragonite particles may suggest that background salts are being trapped during growth, however, Na is not correlated with chloride though this will be further tested through other characterization techniques. In addition, normalisation of the Na and Mg to Ca EDS peak showed that both Na and Mg were higher in the central region than in the rim of the aragonite particle (Supplementary information, Section S1, Sup-Figure 3).

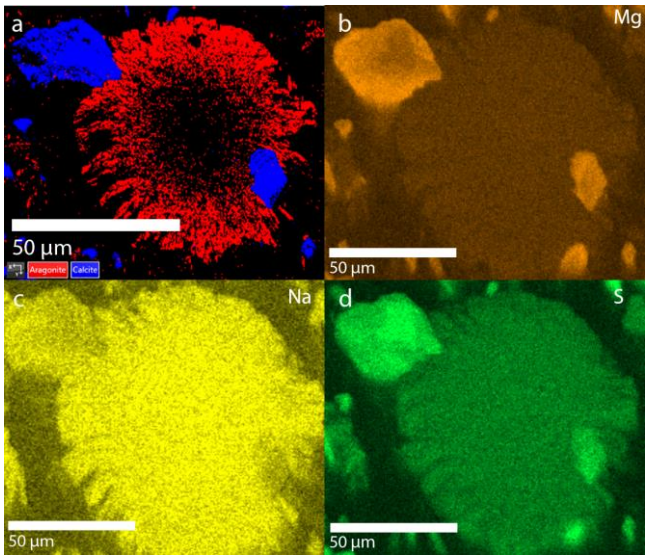

Figure 10. (a) Phase map, and elemental maps for (b) Mg, (c) Na and (d) S obtained from the EBSD analysis for the particles shown in Figure 9 and in (a)

It should be noted that sodium ion incorporation was observed by Branson et. al.[40] and La Fontaine et. al.[41] in tooth enamel. They observed the Mg^{2+} rich amorphous calcium phosphate part of the enamel was also Na^{+} rich. Therefore, it is likely that this is not due to solution inclusion but is a real phenomenon. Aragonite containing Mg^{2+} ions has also been previously observed, however, these studies did not link Mg^{2+} ion (or Na^{+} ion) inclusion as an important mechanism for stabilisation of aragonite.[29]

Crystal Orientation Analysis

The sample used for measuring the EBSD data was further analysed for the orientational relationships between the crystallites found in the aragonite particle. The similar colours on opposite ends of the particle (for both the z and x direction, Figure 11) show that there is a common zone that the aragonite rods grow in. The colour wheels show that for the x and z direction, these preferred orientations are the (010) and (100). For the y direction the (001) and (010) appear more often.

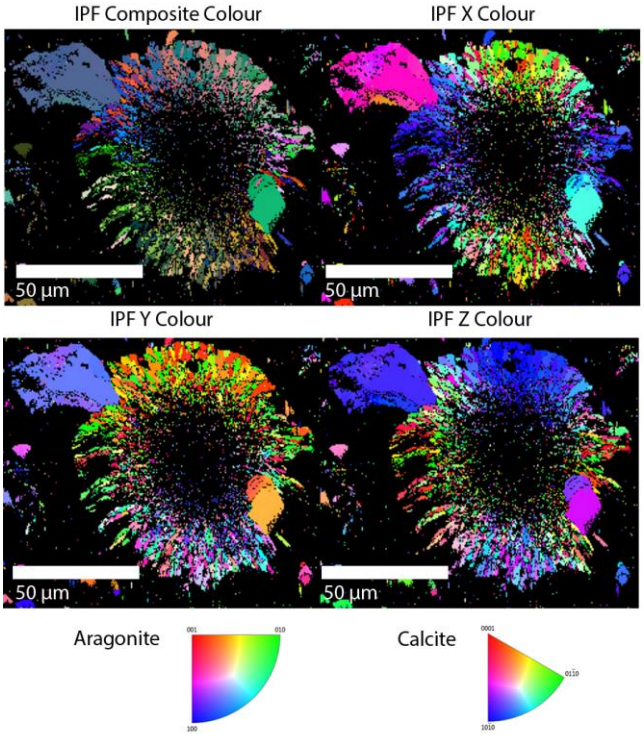

Figure 11. Orientational analysis of particle investigated with EBSD. (a) IPFZ colour orientational map (b) colour and orientation correlation for the maps shown (c) IPFY colour orientational map (d) IPFX colour orientational map.

Figure 12 shows a high resolution EBSD orientational map of the lower rim of another particle, including the pole images and inverse pole images for this region. This section of particle shows that the alignment is just off the (100) direction for the z axis. The alignment of aragonite crystallites rotating around the *a* axis has been observed previously in marine creatures (see Suzuki et al.[62]).

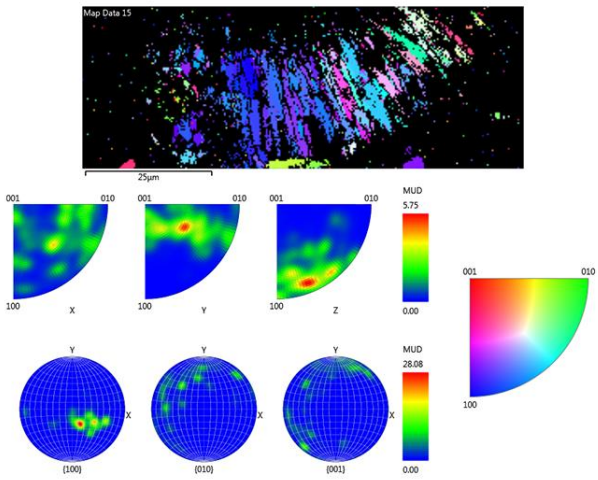

Figure 12. (a) EBSD orientational map of aragonite, (b) pole figures, and (c) inverse pole figures for the section shown in the EBSD orientational map.

High resolution analysis

Particles embedded int~~o~~ resin were used to extract electron transparent lamellae. Two regions of interest (relating to the central and rim area of aragonite particles) were analysed (see Sup-Figure 8 Section 5 of the supplementary information for images of where foils were taken from).

Central region:

The core region of aragonite particles contains nano-crystalline aragonite of approximately 5-10 nm (Figure 13a & b). The crystallinity of these domains can be seen in Figure 13d and the polycrystallinity of the larger section can be observed in Figure 13c. Measurement of the lattice fringes shows that these particles show (002) and (200) distances as found by Zhang[63] and Jiao[64].

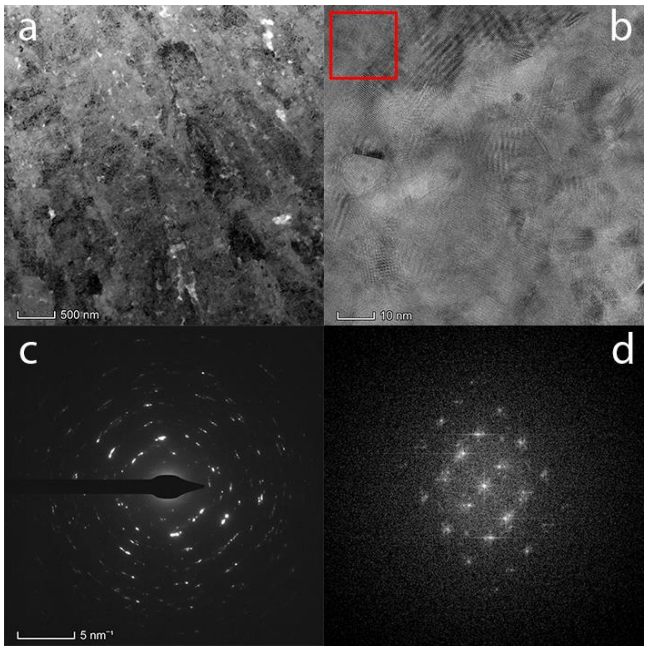

Figure 13. TEM images of (a) Bright field image of the central part of the aragonite particle, (b) higher magnification of (a), (c) SAED patterns of total area shown in (b) while (d) is the Fourier transform from the red box area in (b) (enlarged image of (b) can be found in Sup-Figure 9).

The SAED pattern of a single domain shown in Figure 13 is similar to the zone axis observed by Zhang[63] and Jiao et al.[64] . High magnification imaging (Figure 14) shows that there are sections that have no ordered lattice structure and are amorphous, consistent with EBSD analysis of the core. It suggests that the initially formed aragonite is a mixture of amorphous regions and nano-domained solids, as found by Jiao.[64] It is hypothesised that these crystalline nanodomains are in essence how the crystalline rods are able to form from the centre of the particles.

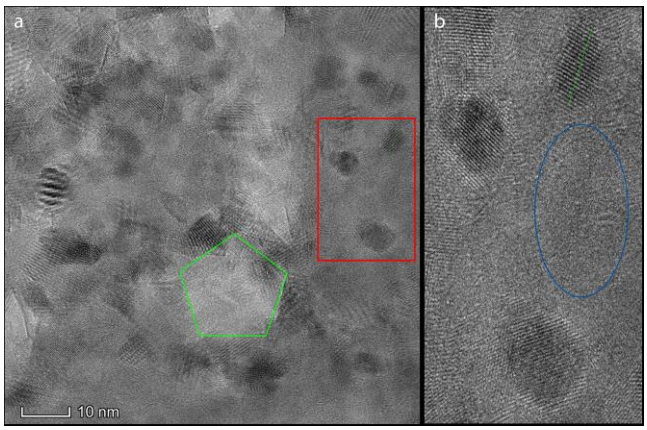

Figure 14. (a) High-resolution bright field TEM image showing crystalline sections and regions that do not appear to have any structure the pentagonal shape highlights void created due to beam exposure (b) zoomed in area of rectangle is shown and oval encloses ‘amorphous’ region.

The structure of the solids was found to alter under the beam. The alteration appeared to be related to the formation of voids, an example of which is shown in Figure 14 by the green polygon. This can be understood as a dehydration reaction due to the ACC having large amounts of water associated with it.[65] Figure 13 shows that this region is littered with 'pockets' of lighter sections in the bright field TEM. No correlation between these lighter sections and any particular element was found and therefore suggests that this is due to gaps within the structure or fluid inclusions. Such holes were also observed by Zhang *et al.*[64]. If these are indeed holes these could be a result of dehydration or could be due to the amorphous to crystalline transition (leading to a solid which is lower in volume).

Rim of particles

The rim of the aragonite crystal, while still being polycrystalline, has much larger crystalline domains of ≥100 nm (Figure 15). Interestingly, there are a significant number of defects (regions of strain, grain boundary dislocations etc., Figure 15b) in these particles. High resolution imaging revealed lattice fringes (Figure 16c) with a spacing of 4.98 Å and this compares well with the *a* axis of aragonite (4.9611 Å). A close up of the interface between two regions shows that the domains align themselves so as to avoid significant lattice mismatch (see supplementary information Section 5, Sup-Figure 9).

Figure 15. Bright field TEM images of the thin foil prepared from the rim of a particle at different magnifications.

There are, other lattice fringe dimensions found showing that there is some variation in the crystal orientation.

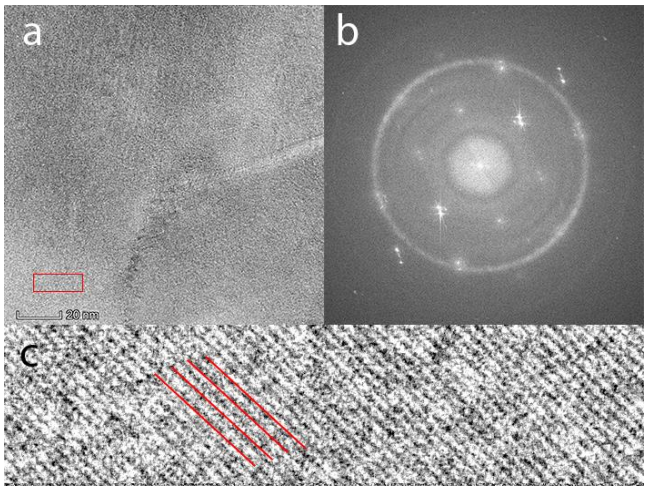

Figure 16. (a) Bright field TEM image of crystalline domain in rim thin section. (b) The Fourier transform of the area corresponds to the (001) zone of aragonite. (c) Area in the box of (a) has been expanded to show lattice fringes more clearly.

Elemental composition of the two regions

EDX on the thin TEM foils found Mg throughout the structure albeit at low levels (Figure 17). There did not seem to be a noticeable accumulation of Mg at grain boundaries dislocations or other defects for the rim part of the particle (Supplementary information, Section 5, Sup-Figure 8). This suggests that the Mg^{2+} ion is substituting for Ca^{2+} rather than incorporating as interstitial impurities or through other mechanisms. For the interior of the particles there is no distinct increase in Mg or S in the darker regions of the HADF image either, thus these dark regions are proposed to be voids rather than solution inclusions. The thin foils investigated by TEM were also used to extract %mass from their EDX spectra.

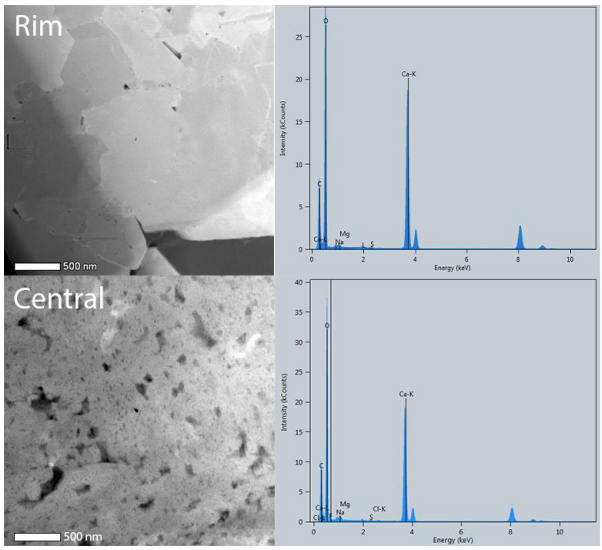

Figure 17. TEM EDX spectra on thin foils created from the interior and rim of the aragonite particles. Note Cu is observed (but not labelled) due to Cu TEM grids being used.

The main difference between the core versus rim section of the particle was that the rim region had significantly more Ca present (~42% c/f 35%) and that the central region of the particle had significantly more impurities in general. In particular, the central region had more magnesium and sulfur (though sodium may be under-represented due to the mobility of Na under the electron beam). The Mg levels (see Table 4) suggest that the ACC might dissolve to form ~~the~~ aragonite (if ACC dissolved lower Mg levels would be expected in the rim as re-crystallization occurs) but this is not supported by the S levels. The level of Na ions was found to be only slightly higher in the core than the exterior of the particle (although this ion could be under-represented as explained previously). It is also interesting to note that the C levels are always higher than expected and that the O levels are lower in the rim of the particle than the central region (possibly due to water being trapped in ACC). Furthermore, it is clear that solution inclusion cannot account for the presence of sodium.

Table 4. Mass % element determined from EDX on TEM thin foil

	Central Region	Rim Region	Expected for Pure $CaCO_3$	Expected for proposed structure*
Ca	35±2.3	42±2.7	40.04	34.4 (C), 38.9 (R)
C	15.9±0.6	15.5±0.9	12.00	11.9 (C), 11.8 (R)
O	48±1.6	42±3.8	47.96	47.9 (C), 47.9 (R)
Mg	0.6±0.7	0.12±0.04		0.5 (C), 0.12 (R)
S	0.16±0.03	0.29±0.05		0.2(C), 0.3 (R)
Na	1.0±0.3	0.60±0.06		2.8(C), 0.46 (R)
Cl	0.1±0.1	Not Detected		
F	0.5±0.2	Not Detected		

*Proposed structures, I=Internal, R=Rim

Errors represent variation found in different regions

C = central region, C structure: $Na_{2z}Mg_xCa_{1-x-z}(CO_3)_{1-y}(SO_4)_y$ where x=0.02, y=0.005 and z=0.06

R = rim region, R structure: $Na_{2z}Mg_xCa_{1-x-z}(CO_3)_{1-y}(SO_4)_y$ where x=0.005, y=0.01 and z=0.01

Molecular simulations

Modeling results showed that substitution of Mg^{2+} into calcite is more energetically favourable than into aragonite. The energy required to substitute an Mg ion into calcite varies from ~0.2-0.8 eV depending on the % substitution. For aragonite the lowest replacement energy at the lowest %Mg ion substitution is already ~0.8 eV. However, while substituting Mg ions appears to be thermodynamically unfavoured for both calcite and aragonite, when sulfate is also present the behaviour altered. Substituting both Mg and sulfate ions into the bulk calcite solids was lower than for aragonite (see Figure 18b) at 0.1% or greater. Modeling supports simultaneous $MgSO_4$ incorporation into calcite. For $MgSO_4$% substitutions between 0.15-0.35 the replacement energy was <0 for calcite meaning this would be thermodynamically favoured. Both aragonite and calcite have similar replacement energies at ~0.08% substitution and below this it is *possible* aragonite has a lower replacement energy than calcite. The incorporation of $MgSO_4$ is seen to follow a linear trend for aragonite in comparison to calcite, however, that could be due to the % substitution range investigated.

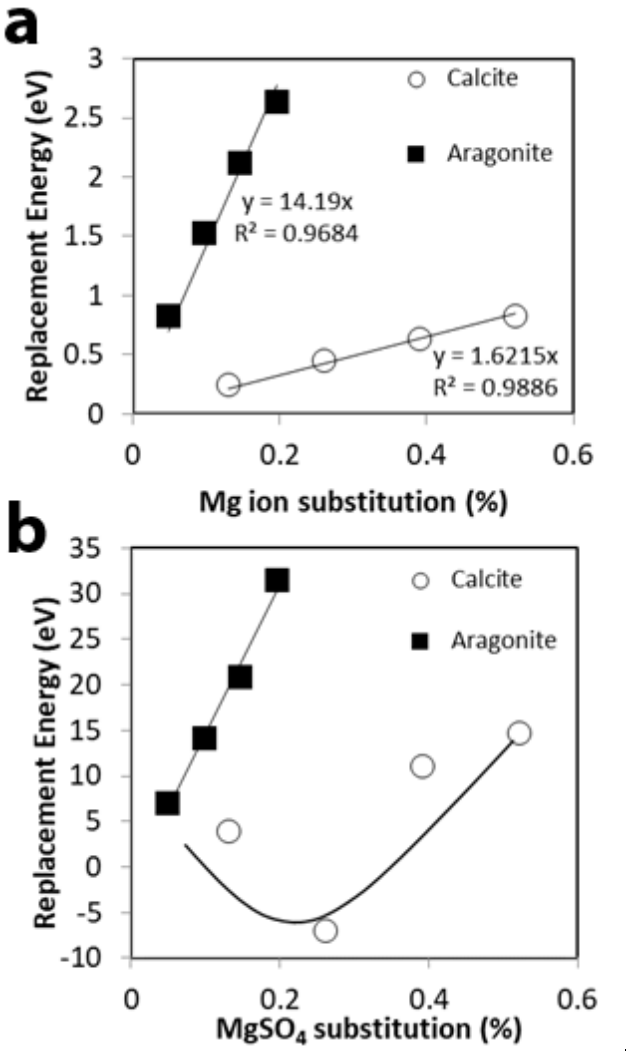

Figure 18. (a) Substitution of Mg^{2+} ions into the aragonite and calcite structure (lines of best fit shown) (b) Substitution of $MgSO_4$ ions into the aragonite and calcite structure (lines drawn to aid reader)

The change in unit cell dimensions of aragonite with the degree of Mg^{2+} and $MgSO_4$ substitution can be seen in Figure 19. The *b* axis length change is not shown as no trend was found with % substitution. When substituting Mg^{2+}, the *a* and *c* axes both shrink with % substitution, but in a non-linear fashion. Substituting $MgSO_4$ units showed the *a* axis decreases but the *c* axis lengthens with $MgSO_4$ content.

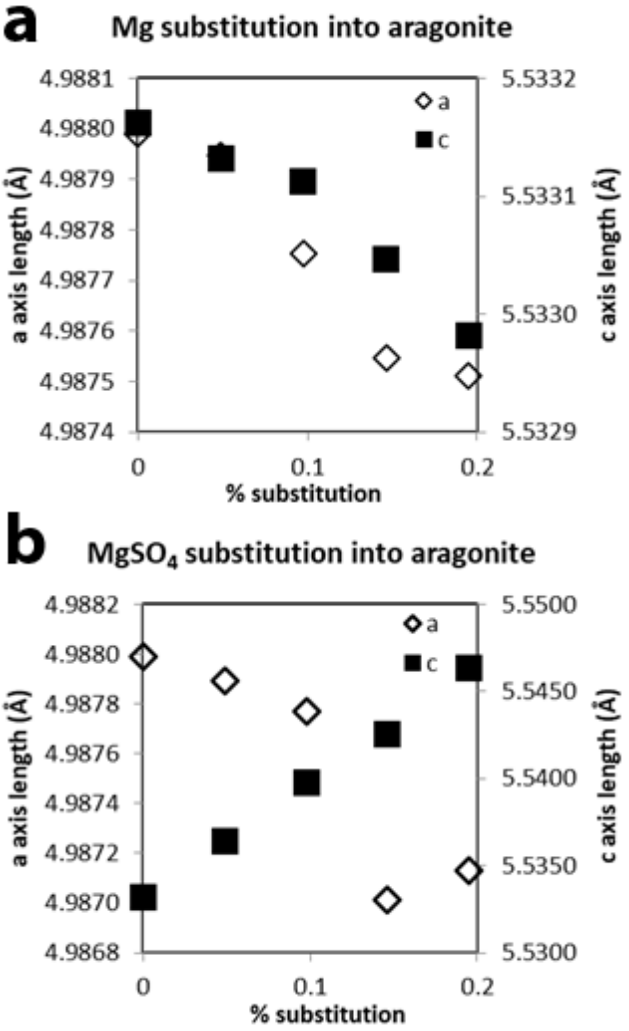

Figure 19. Lattice parameter length (*a* or *c*) versus % substitution for substituting (a) Mg^{2+} ions and (b) $MgSO_4$

Discussion

As can be seen in this work, calcite and aragonite can both form when the driving force is sufficiently high (SI=2). The formation of aragonite is *via* a nanostructured disordered solid (TEM, EBSD data). This supports previous literature that shows aragonite forms through amorphous calcium carbonate (ACC).[66,67] However, this is the first time such conclusive evidence has been presented for a purely synthetic system in the absence of organics or organic solvents. It was also observed that when magnesium ions are present, all nucleation is inhibited and occurs over a longer time-period. It has been hypothesised in the literature that Mg^{2+} ions inhibit calcite formation[29] but these results suggest nucleation of both calcite and aragonite is inhibited. There is previous literature showing the association between Mg^{2+} ions and ACC[8] and this work confirms the presence of the disordered core even in abiotic systems (TEM, EBSD data). Also, sulfate is not necessary for aragonite to be stabilised (see control + Mg^{2+} data).

The formation of aragonite in synthetic seawater, shows that sulfate, sodium and magnesium ions are all incorporated (EBSD). Sulfate is incorporated in both aragonite and calcite – to the point that it is clearly observable in the EDX data (both SEM and TEM samples) and the infrared data. It can be seen that more sulfate substitutes for carbonate in calcite (from the EDX elemental maps). In addition, significant sodium ions are incorporated. This may be due to solution inclusions but the lack of equivalent Cl in the TEM EDX data (particularly at the rim of the particles) and a similar finding in enamel[68] suggests that this is a real effect. The sodium ion appears to be more concentrated in the central disordered region than the rim of the aragonite as found for enamel.[68] Thus, we suggest that the sodium and magnesium ions are an integral part of ACC formation. Sodium ions may play a role in charge stabilization of the ACC-water interactions. This could not be investigated using the thin TEM foils as Na^+ ions can be evaporated from the sample due to the beam energy. Sodium and magnesium ions have similar interactions with sulfate and carbonate and so can become incorporated into the structure through both ions.

Molecular modeling showed that the addition of Mg^{2+} into the aragonite structure is indeed energetically unfavourable. This energy may not be so high in real situations where the surface and the ions are both hydrated and where the incorporation of the Mg^{2+} most likely occurs through ACC. The situation is different when sulfate is also present. In this case the energy of substituting both Mg^{2+} for Ca^{2+} and SO_4^{2-} for CO_3^{2-} is thermodynamically favourable in the calcite structure at concentrations between 0.15-0.35 atom%.

For all of these ions, adsorption is the initial first step, followed by incorporation into the bulk and differences in the kinetics and energetics of this first important step on aragonite and calcite may be the key driver to the differences in the structural substitution contents. Literature[37] has found that for calcite, adsorption and subsequent incorporation both contribute to the inhibition of calcite growth when both Mg^{2+} and sulfate ions are present.

Finally, there is the issue of why the incorporation of such ions results in the stabilisation of aragonite. The thermodynamic enthalpy of formation for aragonite and calcite are very close[69] and aragonite is the denser structure – so initially one would assume that this was the least soluble solid – however, at room temperature, calcite is. Recall, calcite has a dip in solubility with small % Mg substitutions (Figure 2). Thus, just as small amounts of Mg^{2+} ions make calcite less soluble, it may be that the incorporation of $(Mg/Na)SO_4$ units into the aragonite structure lower the solubility of aragonite to below that of pure calcite (and similar in solubility to Mg-calcite). At this point, it is unclear whether the presence of the impurity ions impact the solubility of the solid (thermodynamic stability) or whether it simply slows the transition (kinetic stabilisation). This is an area of current activity.

Conclusions

There are several important conclusions that can be drawn from this work. Firstly, sulfate is not necessary to kinetically stabilise aragonite – magnesium ions are sufficient. Having said that, the presence of sulfate ions appears to increase the relative amount of aragonite that is formed. Secondly, this is not due to surface energy effects on calcite; *all* nucleation is inhibited in the presence of magnesium ions. Thus, magnesium ions adsorbing onto *only* 'calcitic' pre-nucleation clusters can be ruled out as a mechanism of aragonite formation in seawater.

The aragonite initially formed is highly disordered. Nanoparticles with crystallinity exist but are surrounded by amorphous material, ACC. The crystalline nanoparticles are ~5-10 nm in size. Despite popular belief, it is clear that both sodium and magnesium ions incorporate into aragonite in spite of its dense structure. The magnesium ions appear to be substituting into calcium lattice positions. The amorphous core appears to have higher quantities of impurities overall but mostly consists of sodium and magnesium (although the sodium levels may be underestimated). The crystalline aragonite grows or transforms from the amorphous solids in an oriented fashion.

Molecular modeling has shown that substitution of magnesium ions alone is unfavourable in the aragonite and calcite structure but that this changes for calcite when sulfate is also present. While no favourable replacement is seen for aragonite, it may be that other factors may need to be considered. Not least of these is the non-classical transformation of ACC to aragonite. If the Mg ions are trapped in ACC and then the ACC becomes aragonite through a solid-state transformation mechanism the energetics of Mg incorporation of ACC will be critical rather than incorporation into the aragonite structure. This is an area we are exploring.

In terms of aragonite formation in seawater sodium and magnesium ions are hypothesised to be an integral part of ACC and aragonite stabilisation.

ACKNOWLEDGMENTS

We would like to thank and acknowledge the John de Laeter Centre, Curtin University for use of the EM and XRD instrumentation (ARC LE130100053, LE140100150, LE0775551). We would like to also acknowledge the Australian government for funding via the Australian postgraduate award and Curtin University for its use of facilities and equipment.

Supporting Information

Supporting information PDF contains the following sections:
Section 1: Table of experimental conditions; Section 2: EBSD additional information; Section 3: Potentials used in computational simulations; Section 4: Rietveld refinement of structures; Section 5: TEM analysis

REFERENCES

1. Hull, H. & Turnbull, A. G. A thermochemical study of monohydrocalcite. *Geochim. Cosmochim. Acta* **37**, 685–694 (1973).
2. Taylor, G. F. The occurrence of monohydrocalcite in two small lakes in the south-east of South Australia. *Am. Mineral.* **60**, 690–697 (1975).
3. Knigsberger, E., Knigsberger, L.-C. & Gamsjger, H. Carbonates Low-temperature thermodynamic model for the system Na2CO3-MgCO3-CaCO3-H2O. *Geochim. Cosmochim. Acta* **63**, 3105–3119 (1999).
4. Davies, P. J., Bubela, B. & Ferguson, J. Simulation of carbonate diagenetic processes: formation of dolomite, huntite and monohydrocalcite by the reactions between nesquehonite and brine. *Chem. Geol.* **19**, 187–214 (1977).
5. Albéric, M. *et al.* The Crystallization of Amorphous Calcium Carbonate is Kinetically Governed by Ion Impurities and Water. *Adv. Sci.* **5**, 1–9 (2018).
6. Rodriguez-Navarro, C., Kudłacz, K., Cizer, Ö. & Ruiz-Agudo, E. Formation of amorphous calcium carbonate and its transformation into mesostructured calcite. *CrystEngComm* **17**, 58–72 (2015).
7. Beniash, E., Aizenberg, J., Addadi, L. & Weiner, S. Amorphous calcium carbonate transforms into calcite during sea urchin larval spicule growth. *Proc. R. Soc. B Biol. Sci.* **264**, 461–465 (1997).
8. Loste, E., Wilson, R. M., Seshadri, R. & Meldrum, F. C. The role of magnesium in stabilising amorphous calcium carbonate and controlling calcite morphologies. *J. Cryst. Growth* **254**, 206–218 (2003).
9. Paquette, J. & Reeder, R. J. Single-crystal X-ray structure refinements of two biogenic magnesian calcite crystals. *Am. Mineral.* **75**, 1151–1158 (1990).
10. Dickens, B. & Bowen, J. S. Refinement of the crystal structure of the aragonite phase of CaCO3. *J. Res. Natl. Bur. Stand. Sect. A Phys. Chem.* **75A**, 27–32 (1970).
11. Demichelis, R., Raiteri, P., Gale, J. D. & Dovesi, R. The multiple structures of vaterite. *Cryst. Growth Des.* **13**, 2247–2251 (2013).
12. Brecevic, L. & Nielsen, A. E. BRECEVIC 1989.pdf. *J. Cryst. Growth* **98**, 504–510 (1989).
13. Lowenstam, H. A. & Weiner, S. *On Biomineralization*. (Oxford University Press, 1989).
14. Vidavsky, N. *et al.* Calcium transport into the cells of the sea urchin larva in relation to spicule formation. *Proc. Natl. Acad. Sci.* **113**, 12637–12642 (2016).
15. Müller, W. E. G., Schröder, H. C. & Wang, X. The Understanding of the Metazoan Skeletal System , Based on the Initial Discoveries with Siliceous and Calcareous Sponges. *Mar. Drugs Rev.* 172–181 (2017). doi:10.3390/md15060172
16. Anbu, P., Kang, C. H., Shin, Y. J. & So, J. S. Formations of calcium carbonate minerals by bacteria and its multiple applications. *Springerplus* 1–26 (2016). doi:10.1186/s40064-016-1869-2
17. Chang, R. *et al.* Calcium Carbonate Precipitation for CO2 Storage and Utilization: A Review of the Carbonate Crystallization and Polymorphism. *Front. Energy Res.* **5**, 1–12 (2017).
18. Lin, S., Kiga, T., Wang, Y. & Nakayama, K. Energy analysis of CaCO3 calcination with CO2 capture. *Energy Procedia* **4**, 356–361 (2011).
19. Martin, J. B. Carbonate minerals in the global carbon cycle. *Chem. Geol.* **449**, 58–72 (2017).
20. Canon, C., Gattuso, J.-P. & Frankignoulle, M. Marine calcification as a source of carbon dioxide: Positive feedback of increasing atmospheric CO2. *Limnol. Oceanogr.* **39**, 458–462 (1994).
21. Matter, J. M. *et al.* Carbon dioxide emissions for permanent disposal of anthroprogenic carbon dioxide emissions. *Science (80-.).* **352**, 10–13 (2016).
22. Gislason, S. R. *et al.* Rapid carbon mineralization for permanent disposal of anthropogenic carbon dioxide emissions. *Science (80-.).* **352**, 1312–1314 (2016).
23. Zhong, S. & Mucci, a. Calcite and aragonite precipitation from seawater solutions of various salinities: Precipitation rates and overgrowth compositions. *Chem. Geol.* **78**, 283–299 (1989).
24. Mucci, A., Canuel, R. & Zhong, S. The solubility of calcite and aragonite in sulfate-free seawater and the seeded growth kinetics and composition of the precipitates at 25°C. *Chem. Geol.* **74**, 309–320 (1989).
25. Didymus, J. M. *et al.* Influence of low-molecular-weight and macromolecular organic additives on the morphology of calcium

carbonate. *J. Chem. Soc. Faraday Trans.* **89**, 2891–2900 (1993).
26. Addadi, B. L., Raz, S. & Weiner, S. Taking Advantage of Disorder: Amorphous Calcium Carbonate and Its Roles in Biomineralization. *Adv. Mater.* **15**, 959–970 (2003).
27. Blue, C. R. *et al.* Chemical and physical controls on the transformation of amorphous calcium carbonate into crystalline CaCO3 polymorphs. *Geochim. Cosmochim. Acta* **196**, 179–196 (2017).
28. De Yoreo, J. J. Principles of Crystal Nucleation and Growth. *Rev. Mineral. Geochemistry* **54**, 57–93 (2003).
29. Morse, J. W., Arvidson, R. S. & Lüttge, A. Calcium carbonate formation and dissolution. *Chem. Rev.* **107**, 342–381 (2007).
30. Davis, K. J., Dove, P. M. & De Yoreo, J. J. The Role of Mg2+ as an Impurity in Calcite Growth. *Science (80-.).* **290**, 1134 LP – 1137 (2000).
31. Sun, W., Jayaraman, S., Chen, W., Persson, K. A. & Ceder, G. Nucleation of metastable aragonite CaCO 3 in seawater . *Proc. Natl. Acad. Sci.* **112**, 3199–3204 (2015).
32. Railsback, B. L. *Some Fundamentals of Mineralogy and Geochemistry*. *Department of Geology, University of Georgia Athens, Georgia 30602-2501 U.SA.* (University of Georgia, 2006). doi:10.1021/jp981070j
33. Kawano, J., Shimobayashi, N., Miyake, A. & Kitamura, M. Precipitation diagram of calcium carbonate polymorphs: Its construction and significance. *J. Phys. Condens. Matter* **21**, 1–6 (2009).
34. Söhnel, O. & Mullin, J. . A METHOD FOR THE DETERMINATION OF PRECIPITATION INDUCTION PERIODS. *J. Cryst. Growth* 377–382 (1982). doi:10.1109/TPAS.1982.317638
35. Möller, P. & Rajagopalan, G. Charges of excess free energies in the crystal growth process of calcite and aragonite due to the presence ofMg2+ ions in solution. *Z. Phys. Chem.* 187 (1979).
36. Li, Q., Fernandez-Martinez, A., Lee, B., Waychunas, G. A. & Jun, Y. S. Interfacial energies for heterogeneous nucleation of calcium carbonate on mica and quartz. *Environ. Sci. Technol.* **48**, 5745–5753 (2014).
37. Nielsen, M. R. *et al.* Inhibition of Calcite Growth: Combined Effects of Mg2+ and SO42−. *Cryst. Growth Des.* **16**, 6199–6207 (2016).
38. Reddy, M. M. & Nancollas, G. H. The crystallization of calcium carbonate IV: the effect of magnesium, strontium and sulfate ions. *J. Cryst. Growth* **35**, 33–38 (1976).
39. Helnwein, P., Mang, H. A. & Pichler, B. Ab initio estimates of stability limits on nonlinear load-displacement paths: Potential and limitations. *Comput. Assist. Mech. Eng. Sci.* **6**, 345–360 (1999).
40. Branson, O. *et al.* Nanometer-Scale Chemistry of a Calcite Biomineralization Template: Implications for Skeletal Composition and Nucleation. *Proc. Natl. Acad. Sci.* **113**, 12934–12939 (2016).
41. Fontaine, A. La *et al.* Atomic-scale compositional mapping reveals Mg-rich amorphous calcium phosphate in human dental enamel. *Sci. Adv.* **2**, 1–6 (2016).
42. Berges, J. A., Franklin, D. J. & Harrison, P. J. Evolution of an artificial seawater medium: Improvements in enriched seawater, artificial water over the last two decades. *J. Phycol.* **37**, 1138–1145 (2001).
43. Hart, R. J. W. J. J. B. D. J. and F. M. E. *Water-Resources Investigations Report 02-4026*. (2002).
44. Arvidson, R. S. & Mackenzi, F. T. The dolomite problem; control of precipitation kinetics by temperature and saturation state. *Am. J. Sci.* **299**, 257–288 (1999).
45. Parkhurst, B. D. L. User's Guide to pHREEQ a Computer Program for Speciation, Reaction-Path, Advective-Transport, and Inverse Geochemical Calculations. *U.S. Geol. Surv.* 1–22 (1995).
46. Boon, M. & Jones, F. Barium Sulfate Crystallization from Synthetic Seawater. *Cryst. Growth Des.* **16**, 4646–4657 (2016).
47. Raiteri, P., Demichelis, R. & Gale, J. D. Thermodynamically Consistent Force Field for Molecular Dynamics Simulations of Alkaline-Earth Carbonates and Their Aqueous Speciation. *J. Phys. Chem. C* **119**, 24447–24458 (2015).
48. Byrne, E. H., Raiteri, P. & Gale, J. D. Computational Insight into Calcium − Sulfate Ion Pair Formation. *J. Phys. Chem. C.* **121**, 25956–25966 (2017).
49. Fleming, S. & Rohl, A. GDIS: A visualization program for molecular and periodic systems. *Z Kryst* **220**, 580–584 (2005).
50. Gale, J. D. & Rohl, A. L. The General Utility Lattice Program. *Mol. Simul.* **29**, 291–341 (2003).
51. Taylor, P., Sabbides, T., Giannimaras, E. & Koutsoukos, P. G. The precipitation of calcium carbonate in artificial seawater at sustained supersaturation. *Environ. Technol.* **13**, 73–80 (1992).
52. Rushdi, A. I. Mineralogy and Morphology of Calcium Carbonate as a Function of Magnesium Concentration in Artificial Seawater. *J. Mar. Sci. Eng.* **3**, 13–24 (1992).
53. Kartnaller, V., Ribeiro, E. M., Venancio, F., Rosario, F. F. & Cajaiba, J. Preferential incorporation of sulfate into calcite polymorphs during calcium carbonate precipitation: An experimental approach. *CrystEngComm* **20**, 2241–2244 (2018).
54. Fernandez-Diaz, L., Putnis, A., Prieto, M. & Putnis, C. V. The role of magnesium in the crystallization of calcite and aragonite in a porous medium. *J. Sediment. Res.* **66**, 482–491 (1996).
55. Parkman, R. H., Charnock, J. M., Livens, F. R. & Vaughan, D. J. A study of the interaction of strontium ions in aqueous solution with the surfaces of calcite and kaolinite. *Geochim. Cosmochim. Acta* **62**, 1481–1492 (1998).
56. Mass, T. *et al.* Amorphous calcium carbonate particles form coral skeletons. *PANS* 114–123 (2017). doi:10.1073/pnas.1707890114
57. Holcomb, M., Cohen, A. L., Gabitov, R. I. & Hutter, J. L. Compositional and morphological features of aragonite precipitated experimentally from seawater and biogenically by corals. *Geochim. Cosmochim. Acta* **73**, 4166–4179 (2009).
58. Pokroy, B. *et al.* Atomic structure of biogenic aragonite. *Chem. Mater.* **19**, 3244–3251 (2007).
59. Lowenstam, H. A. & Series, N. Minerals Formed by Organisms Heinz A. Lowenstam. **211**, 1126–1131 (1981).
60. Wu, S., Chiang, C.-Y. & Zhou, W. Formation Mechanism of CaCO3 Spherulites in the Myostracum Layer of Limpet Shells. *Crystals* **7**, 319 (2017).
61. Finch, A. A. & Allison, N. Coordination of Sr and Mg in calcite and aragonite. *Mineral. Mag.* **71**, 539–552 (2008).
62. Suzuki, M., Sasaki, T., Oaki, Y. & Imai, H. Stepwise rotation of nanometric building blocks in the aragonite helix of a pteropod shell. *Cryst. Growth Des.* **17**, 191–196 (2017).
63. Zhang, J., Yan, J. & Sheng, J. Nanoscale structure and formation mechanism of the aragonite fibers in the ligament of Hyriopsis Cumingii shell. 3383–3390 (2015). doi:10.1007/s10853-015-8894-3
64. Jiao, D., Liu, Z., Zhang, Z. Z. & Zhang, Z. Z. Intrinsic hierarchical structural imperfections in a natural ceramic of bivalve shell with distinctly graded properties. *Sci. Rep.* **5**, 1–13 (2015).
65. Huang, S. C., Naka, K. & Chujo, Y. A carbonate controlled-addition method for amorphous calcium carbonate spheres stabilized by poly(acrylic acid)s. *Langmuir* **23**, 12086–12095 (2007).
66. Walker, J. M., Marzec, B. & Nudelman, F. Solid-State Transformation of Amorphous Calcium Carbonate to Aragonite Captured by CryoTEM. *Angew. Chemie - Int. Ed.* **56**, 11740–11743 (2017).
67. MacIás-Sánchez, E., Willinger, M. G., Pina, C. M. & Checa, A. G. Transformation of ACC into aragonite and the origin of the nanogranular structure of nacre. *Sci. Rep.* **7**, 1–11 (2017).
68. La Fontaine, A. *et al.* Atomic-scale compositional mapping reveals Mg-rich amorphous calcium phosphate in human dental enamel. *Sci. Adv.* **2**, (2016).
69. Lide, D. R. *Selected Values of Chemical Thermodynamic Properties*. *A Century of Excellence in MEASUREMENTS, STANDARDS, and TECHNOLOGY* **270**, (U.S Department of Commerce, 2018).